RESEARCH ARTICLE

**ADVANCED
PHYSICS
RESEARCH**
Open Access

www.advphysicsres.com

Quantifying Output Power and Dynamic Charge Distribution in Sliding Mode Freestanding Triboelectric Nanogenerator

Xin Guo, Jiajia Shao, Morten Willatzen, Xiaolin Wang, and Zhong Lin Wang*

The general concept of dielectric polarization density (P) is a macroscopic description of the underlying microscopic structure in the presence of an external electric field and polarized materials itself. A time-dependent polarization P_S induced by a non-electric field also exists in practice due to the mechanically driven relative motion of media owing to the effects of contact electrification or piezoelectricity. In this work, the starting point is to consider the difference between P and P_S, and how P_S enters into the governing equations, since it describes the dielectric polarization density without an applied electric field, finally modifying the constitutive relations, Faraday's law, and Maxwell's equations. On this background, a 3D mathematical-physical model for the sliding mode freestanding triboelectric nanogenerators (TENGs) is established that is taken as an example to confirm the relationship of free charge distribution and dynamics of output power. What needs to be emphasized is that the method of segmented uniform charge distribution is effective and the physical basis for modeling construction and analysis. Finally, we summarized the mathematical-physical models of TENGs in rectangular coordinates, cylindrical coordinates, and spherical coordinates, building a bridge to reveal the underlying principle behind the microscopic polarization and energy conversion.

1. Introduction

The generation of electromagnetic energy is a non-conservative process when we consider the energy conversion system associated with an external energy source. For instance, the triboelectric nanogenerator (TENG) is a novel alternating current (ac) electricity generator which is based on a time-varying electric polarization of dielectric materials without an applied electric field.[1–6] An external energy input such as mechanical energy is essential during the generation of electricity. Therefore, to understand the dynamic evolutions of the electromagnetic field, the classical Maxwell's equations should be expanded with the consideration of an external energy source.[7–10] This means that the form of Maxwell's equations must be extended with an appropriate redefinition of some physics quantities. Against it should be noticed that the Maxwell-Faraday law cannot explain the generation of electromotive force in TENGs since there is no obvious change of magnetic flux when converting the mechanical energy into electricity. In general, the force due to the external energy source acts on each free and bound charge which provides a non-conservative electromotive force, finally producing electricity.[11–13]

The external energy source mainly comes in two types: electric energy sources and non-electric energy sources.[11–13] Regarding the former as an ideal voltage generator or battery produces a direct current (dc) voltage and an electric field directly, the force per unit charge due to the external energy source enables the electrons to move in the opposite direction, realizing the separation of opposite polarity charges within the voltage source.[11–14] The

X. Guo, J. Shao, M. Willatzen, Z. L. Wang
Beijing Institute of Nanoenergy and Nanosystems
Chinese Academy of Sciences
Beijing 101400, P. R. China
E-mail: zlwang@gatech.edu

X. Guo, J. Shao, M. Willatzen, Z. L. Wang
School of Nanoscience and Technology
University of Chinese Academy of Sciences
Beijing 100049, P. R. China

X. Wang
Institute for Superconducting and Electronic Materials
University of Wollongong
Wollongong, New South Wales 2500, Australia

Z. L. Wang
School of Materials Science and Engineering
Georgia Institute of Technology
Atlanta, Georgia 30332-0245, USA

**ADVANCED
SCIENCE NEWS**

www.advancedsciencenews.com

**ADVANCED
PHYSICS
RESEARCH**
Open Access

www.advphysicsres.com

non-electric energy source provides a force on the electric charges which requires generalization of the constitutive relations and results in a modification of Maxwell's equations.[11,12] The above approach has been utilized to investigate the dc bound-charge voltage source which is essentially a bar electret.[15–18] The electret exhibits a quasi-permanent electric field due to its macroscopic polarization; and it is overall electrically neutral.[15–18] So, there is no free charge or current within the system, thus the divergence of electric flux density (D) and the curl of the electric field density must be zero. For a general linear electret, the relationship of D and electric field E becomes[11]:

$$\mathbf{D} = \varepsilon_0 \mathbf{E} + \varepsilon_0 \chi \mathbf{E} + \mathbf{P}_b^i \tag{1}$$

where ϵ_0, and χ represent the vacuum permittivity and electric susceptibility respectively; and $\mathbf{P}_b^i$ is the permanent polarization that is independent of E. It should be noticed that the divergence of E is nonzero, because of the physical separation of bound charges $\rho_{b_{Pi}}$. Then[11]:

$$\varepsilon_0 \varepsilon_r \nabla \cdot \mathbf{E} = -\nabla \cdot \mathbf{P}_b^i = \rho_{b_{Pi}} \tag{2}$$

The dc voltage source ($\mathcal{E}$) can be obtained through the integral of the whole circuit, which gives

$$\varepsilon = \frac{1}{\varepsilon_0 \varepsilon_r} \oint \mathbf{P}_b^i \cdot d\mathbf{l} \tag{3}$$

Different from the dc bound-charge voltage source, a polarization vector term $\mathbf{P_S}$ has been introduced in the displacement vector D to clarify the energy conversion process of TENGs and piezoelectric nanogenerators (PENGs).[7–10,19,20] For the TENG, the pre-existing electrostatic charges play a key role in the generation of $\mathbf{P_S}$. Here the electrostatic charge is a triboelectric charge which is a non-movable free charge.[21–24] These charges are created during the contact-separation process between media and cannot move freely in a macroscopic way since they are distributed in the dielectrics.[25–27,28–30] The triboelectric charges generate the electric field which then polarizes dielectric materials, and this polarization will produce its own electric field, thereby contributing to the total electric field, and in turn updates the total polarization. The end result for the electric displacement D in linear media becomes[7–10]:

$$\mathbf{D} = \varepsilon_0 \mathbf{E} + \mathbf{P} + \mathbf{P_S} \tag{4}$$

Note that here the E is the total electric field, not that portion generated by the polarization or an external electric field. Therefore, the electric Gauss law is modified as:

$$\nabla \cdot \mathbf{D}' = \rho_f - \nabla \cdot \mathbf{P_S} \tag{5}$$

where ρ_f is the free charge density. Here we make a substitution of D' by $D = D' + P_S$. The corresponding integral form reads:

$$\oint_S \mathbf{D}' \cdot d\mathbf{S} = Q_{\text{free}} \tag{6}$$

where Q_{free} denotes the total free charge enclosed in the volume. This approach is useful and widely appreciated for dielectric media because it only involves free charges that we can control. There are two kinds of free charges in a TENG device: triboelectric charges distributed in the dielectric media and free movable charges on the electrodes. Experimentalists have stressed that triboelectric charges are the key to all of them.[7,31] The purpose of this article is to thoroughly elucidate the relationship between the charge distributions and dynamics of the energy conversion process of TENGs.

In this work, we will exhibit the relationships between the free charge distribution and dynamics of energy conversion, taking the sliding mode freestanding triboelectric nanogenerator (SF-TENG) as an example. Since the free movable charges distributed on the electrodes of a SF-TENG are non-uniform and time-dependent, the complete charge distribution is still a mystery. A detailed and accurate mathematical-physical model describing the dynamics of the energy conversion process of the SF-TENG is lacking to this day, although they have been applied widely in engineering.[32–34] In this work, a 3D mathematical-physical model of SF-TENGs is established that allows us to analyze the relationships between free charge distribution and output characteristics. In particular, variations of the electric potential, electric field, displacement current, output power, and quasi-electrostatic energy at different conditions are revealed. Further, the present approach summarizes the physical models of TENGs with various geometry structures and free charge distributions. Note that the research framework and approaches discussed in this work are also useful for other modes of TENGs. Against this background, it is then very fitting to conclude that utilizing the time-varying polarization (physical dipole) to generate electricity is the physical essence of TENGs.

2. General Theory and Modeling

As stated before, the vector $\mathbf{P_S}$ represents an additional source for polarization of the dielectric materials, and the corresponding generated bound current ($\mathbf{J}_{sb}$) is obtained by

$$\nabla \times \mathbf{P_S} = -\varepsilon_0 \varepsilon_r \mathbf{J}_{sb} \tag{7}$$

Due to the additional term $\mathbf{P_S}$ and the added magnetic current boundary source, classical Maxwell's equations could be generalized as

$$\nabla \cdot \mathbf{D}' = \rho_f - \nabla \cdot \mathbf{P_S} \tag{8a}$$

$$\nabla \cdot \mathbf{B} = 0 \tag{8b}$$

$$\nabla \times \mathbf{E} = -\frac{\partial \mathbf{B}}{\partial t} \tag{8c}$$

$$\nabla \times \mathbf{H} = \mathbf{J}_f + \frac{\partial \mathbf{D}'}{\partial t} + \frac{\partial \mathbf{P_S}}{\partial t} \tag{8d}$$

where B is the magnetic flux density, $\mathbf{J}_f$ is the free electric current density and the material is assumed non-magnetic. If the polarization has curl, the displacement field does, as observed in Equation (8c). For a TENG device, the origin of the total force per unit charge E is the free movable charges distributed on the electrodes and free non-movable charges in dielectrics. Subsequently,
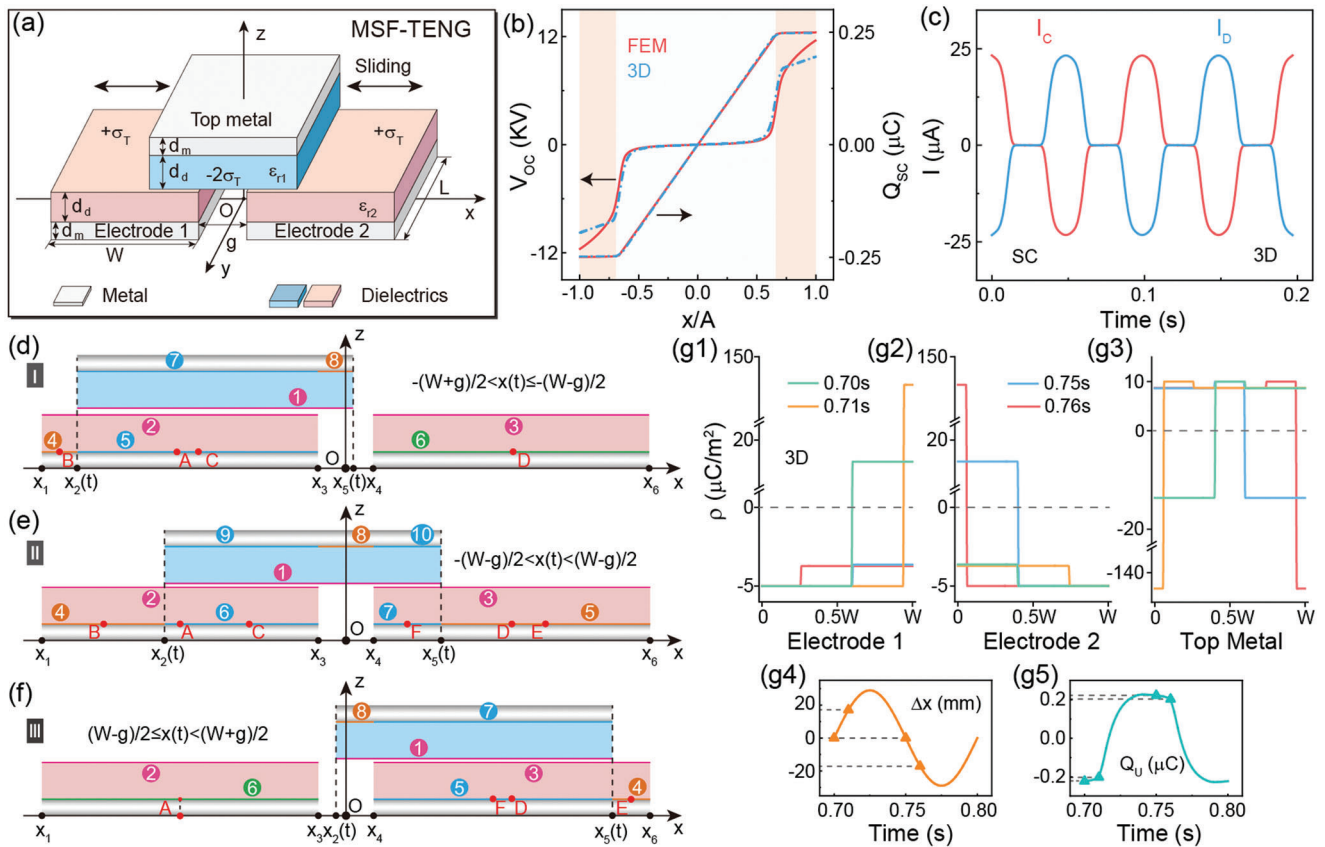
Figure 1. Basic output characteristics of the MSF-TENG. a) Structural schematic diagram of the MSF-TENG. b) V_{OC} and Q_{SC} with respect to the ratio x/A. c) Conductive current and displacement current changing with time. Schematic diagram of the charge distribution for MSF-TENG in d) Region I, e) II and f) III, respectively. g) The charge distributions at electrodes, top metal, and transferred charges in a steady cycle when an optimum resistor ($R_{opt} = 3.15 \times 10^8 \Omega$) is connected.

it leads to the production of potential difference of TENGs. On the other hand, the dielectric polarization P_S introduced by a non-electric field can be regarded as a voltage source inside the medium but does not exist outside it. As demonstrated in Equation (4), the constitutive relations are modified due to the microscopic polarization P_S as are Faraday's law and Maxwell's equations.

Furthermore, there are differences between permanent polarization $\mathbf{P}_b^i$ and redefined polarization P_S. The permanent polarization $\mathbf{P}_b^i$, essentially a part of the traditional polarization, is usually generated through an external electric field. The term P_S is produced due to mechanical excitation which is independent of an external electric field. On the other hand, the macroscopic polarization $\mathbf{P}_b^i$ is often found in an ideal bar electret which can be maintained over a long time due to the permanent bound charges; but P_S can disappear in the absence of electrostatic charges. Microscopically, P_S is introduced to describe the polarization degree of dielectrics that is equal to the dipole moment per unit volume. It should be clear that the potential (and thus the corresponding electric field) of a polarized material is the same as that produced by a volume charge density $\rho_b = -\nabla \cdot \mathbf{P}$ plus a surface charge density $\sigma_b = -\mathbf{P} \cdot \mathbf{n}$. Both the volume charges and surface charges are designated bound charges. This is why we stress that an associated external energy source should be ap-

plied to separate positive and negative charges for the generation of induced dipole moments. So, the general polarization P and permanent polarization $\mathbf{P}_b^i$ come from the external electric field, while the additional term P_S is due to the pre-existing electrostatic charges caused by external mechanical excitation. In other words, the various sources for polarization contributions are different.

Because a TENG device is usually operated at low frequency magnetic fields are extremely weak, such that $\nabla \times \mathbf{E} \approx 0$. Then, the total electric field $\mathbf{E}$ can be identified by a scalar potential ϕ: $\mathbf{E} = -\nabla\phi$. The details of how to obtain the electric field and electric potential of TENGs have been proposed in our previously published articles.[19–23] Here, we put our focus on the SF-TENG energy harvesting device. It is worth highlighting that the physical laws do not depend on the choice of coordinate systems used in a mathematical model but the quantitative relationships among physical quantities must be uniquely described in any mathematical model. A 3D mathematical-physical model is present from which we could explore how the sources (such as the free charges) affect the spatial-temporal behavior of electromagnetic fields for a SF-TENG device and the relevant energy conversion process. Two typical metals SF-TENG (MSF-TENG) and dielectric SF-TENG (DSF-TENG) are demonstrated in **Figure 1**a, respectively, which are classified based on the charge distribution and geometry structure. As the sliding part moves left and right

**ADVANCED
SCIENCE NEWS**
www.advancedsciencenews.com

**ADVANCED
PHYSICS
RESEARCH**
Open Access
www.advphysicsres.com

under a mechanical excitation, free charges are produced that flow between electrodes 1 and 2 to keep electrostatic equilibrium; electricity is converted and outputted in the external circuit during the sliding process. At the same time, redistribution of induced free charges is observed in the top metal. This is a comprehensive energy conversion process which may be difficult to understand owing to a scarcity of details. For instance, we must be conscious of how the polarization of dielectric material changes under the time-varying electric field generated by the dynamics of charge distributions both at the contacting surfaces and the electrodes.

Since the highly asymmetric geometry structure and the air gap between the two electrodes which affect the divergence of the electric field, the charge distributions are divided into three states according to the position ($x(t)$) of the sliding part (Figure 1d). It is apparent that in state I: $-(W+g)/2 < x(t) \leq -(W-g)/2$, state II: $-(W-g)/2 < x(t) < (W-g)/2$, and state III: $(W-g)/2 \leq x(t) < (W+g)/2$, where W and g represent the width of the dielectric and air gap, respectively. Each Arabic number represents a special charged surface, such as the starting point and endpoint of different electrodes are set as x_1, $x_2(t)$, x_3, x_4, $x_5(t)$, and x_6, respectively (Figure 1d). As the top metal moves from left to right; or conversely, $x_2(t)$, and $x_5(t)$ change with time. The details of charge distributions are illustrated in Appendix A. They are based on the following principles or assumptions: a) the MSF-TENG is neutral at any time, thus it can be regarded as a lumped element due to the lumped matter discipline (LMD); b) the free charges are segmented and distributed uniformly on the electrodes; c) the electric potential of the electrode is evaluated through some special points, since it is difficult to establish an equipotential for the metal electrode in term of boundary conditions of quasi-electrostatics. So, the MSF-TENG device has been modeled as a highly complex system with a complicated charge distribution and the special ability of self-regulatory to be neutral during the energy conversion process.

As stated above, once the charge distributions are confirmed, the corresponding electric potential can be evaluated by the equations given in Appendix B. Note that a representative point is located at the intersection between the perpendicular bisector of the charged surface and the electrode. There are three cases we should consider. First, all free charges (Q_U) can be transferred from one electrode to the other at short-circuit (SC) conditions; consequently, the electric potentials of the two electrodes are equal to each other, i.e., $\phi_1(t) = \phi_2(t)$, where $\phi_1(t)$ and $\phi_2(t)$ represent the electric potential of electrode 1, and electrode 2, respectively. In the open-circuit (OC) case, no free charges are transferred between the two electrodes, thus $-V_{OC} = \phi_1(t) - \phi_2(t)$, where V_{OC} represents the open-circuit voltage of the SF-TENG. When an external resistor (Z_L) is connected, the time-varying charge transfer is determined by $-Z_L \frac{dQ_U}{dt} = \phi_1(t) - \phi_2(t)$. This governing equation is a first-order linear differential equation that can be solved to determine the time-variant physical quantities of the TENG device.

3. Results and Discussion

Numerical calculations from the 3D model and the finite element simulation (FEM) have been carried out. The corresponding modeling parameters are shown in **Table 1**. As demonstrated

Table 1. Simulation parameters and materials for the 2D simulations using COMSOL software.

Structure	Parameters
Metals	Aluminum
Dielectric 1	Custom material, $\epsilon_{r1} = 2$
Dielectric 2	Custom material, $\epsilon_{r2} = 3$
Thickness of metal electrodes, d_m	20 μm
Thickness of dielectric layers, d_d	100 μm
Width of dielectrics and metals, W	0.05 m
Width of air gap between electrodes, g	0.01 m
Vertical gap between dielectric 1 and 2	10^{-5} m
Side length of a square air domain, a	4 m
Charge density on the lower surface of dielectric 1	-10 μC m^{-2}
Charge density on the upper surfaces of dielectric 2	5 μC m^{-2}

in Figure 1b, the variations of V_{OC} and Q_{SC} calculated using the 3D model are similar to those of the results from the FEM model, indicating the correctness and precision of the built 3D mathematical-physical model. It should be noticed that in state II, Q_{SC} is proportional to the relative position (x/A, where A is equivalent to $g/2 + W/2$) of the sliding part, and the variation of V_{OC} is consistent with the theoretical results reported in Reference 32. Moreover, the SC current and the displacement current ($I_{D,SC}$) are the same in magnitude except in opposite directions (Figure 1c).

As the sliding part moves subject to a continuous external excitation using an optimum value of the resistor, the variations of the quasi-electromagnetic field of MSF-TENG will cause free charge redistribution in the electrodes (Figure 1g). When $x/A = 0$ (state II, Figure 1e) the free charge density (σ) at the non-overlapped regions (represented by No. 4, 5) of the upper surfaces of the electrode 1 and electrode 2 is equal to $-\sigma_T$ (-5 μC/m^2) while that of at the top electrode (No. 8) is close to $2\sigma_T$ (10 μC/m^2). The charge distributions in the overlapped regions are more complex than those in the non-overlapped regions. Opposite electrical charges are distributed in the No. 6 region compared to those in the No. 4 region, and the corresponding σ is smaller than 20 μC/m^2; interestingly, in the No.7 region, like charges are induced, and the relevant σ is larger than that of at the non-overlapped region (No.5). This means that the total charge at the upper surface of electrode 2 is negative when the charge at electrode 1 is positive. The imbalance is an outcome of transferred charges between the two electrodes; however, the total amount of charge distributed in the electrodes remains the same and may be zero or a constant but it doesn't change during the energy conversion process.

Furthermore, the induced charges in the lower surfaces of the top metal at regions No. 9 and No. 10 have opposite signs since they are largely affected by the total charges contained in the two electrodes. For instance, the total amount of charge in electrode 2 is negative, thus to maintain dynamic equilibrium the free charges induced in region No. 10 must be positive (Figure 1g3). Note that net induced charge in the top metal is zero at any time because no charges are transferred in or out during the energy harvesting process except for connecting an external
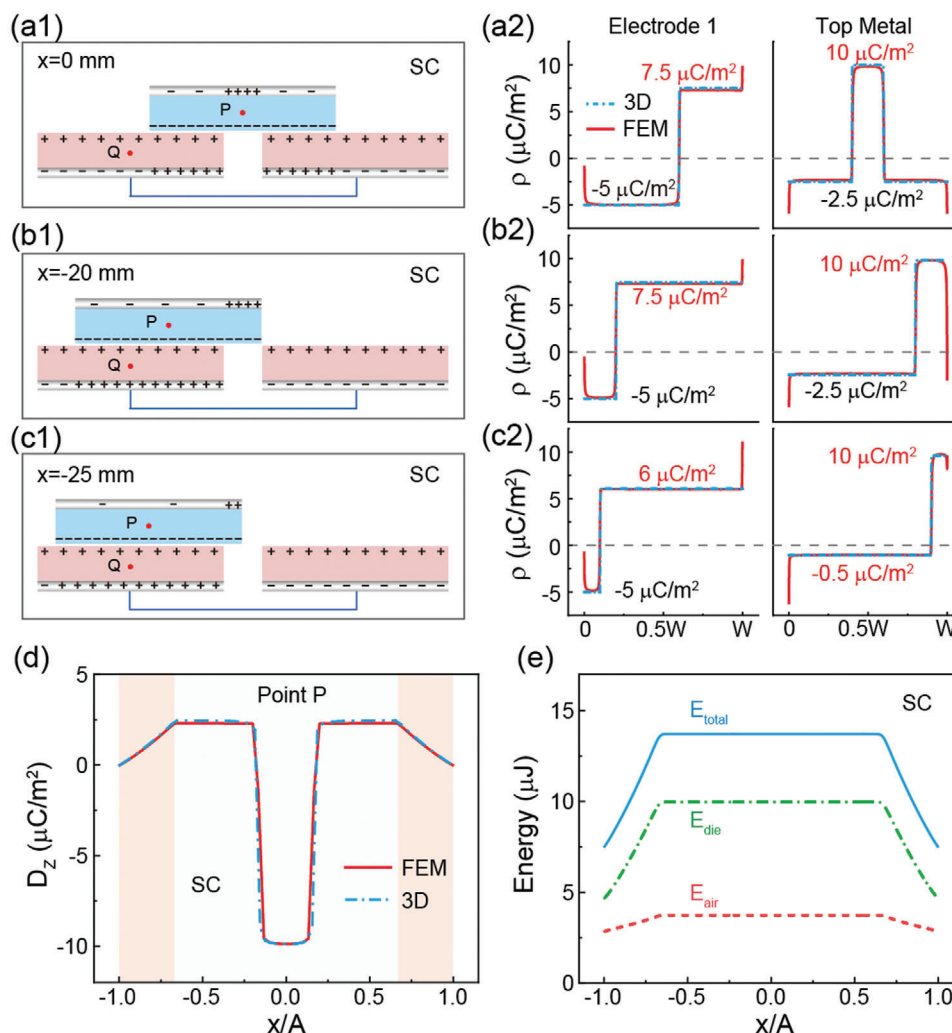
ADVANCED
SCIENCE NEWS

www.advancedsciencenews.com

ADVANCED
PHYSICS
RESEARCH
Open Access

www.advphysicsres.com

Figure 2. Output characteristics of the MSF-TENG at SC conditions. Schematic diagram of the sliding part and charge distributions at a) $x = 0$ mm, b) -20 mm, and c) -25 mm, respectively. d) D_z at point P with respect to the ratio x/A. e) Electrostatic energy distributed in the dielectric, air, and total electrostatic energy of the system at SC conditions.

circuit. Quantitatively, the charge densities at the overlapped regions of No. 6 and 7 are calculated by: $\sigma_6 = -Q_U/W_{11} + \sigma_T W_{10}/W_{11}$, and $\sigma_7 = Q_U/W_{21} + \sigma_T W_{20}/W_{21}$, where $W_{10} = x_2(t)-x_1$, $W_{11} = x_3-x_2(t)$, $W_{20} = x_6-x_5(t)$, and $W_{21} = x_5(t)-x_4$, respectively. For the regions of No. 9 and 10, they can be confirmed by: $\sigma_9 = \sigma_T - \sigma_T W_{10}/W_{11} + Q_U/W_{11}$, and $\sigma_{10} = \sigma_T - \sigma_T W_{20}/W_{21} - Q_U/W_{21}$, respectively. Details are demonstrated in Appendix A.

In addition, when the sliding part moves to the right and close to $x/A = 0.59$ (0.71 s), the electrons will follow moving from electrode 2 to electrode 1 continuously until reaching a new equilibrium state (Figure 1g). As a result, negative charges are transferred to electrode 1, and the induced charge at the region of No. 6 changes from positive to negative; meanwhile, less negative charge (or more positive charges) is distributed in the overlapped region of No. 5. Conversely, if the sliding part moves to the left $x/A = -0.59$ (0.76 s), a mirror symmetry charge distribution is observed in Figure 1g, which is mainly due to the electrons transferred from electrode 1 to electrode 2 to maintain electrical neutrality of the TENG device. Some basic conclusions can be

obtained from the above analysis: 1) the charge density σ at the non-overlapped region of electrodes never changes as the sliding part moves but it has an opposite sign compared to that of the corresponding contacting surface; 2) although both positive and negative charges are distributed on one electrode, the total charge is exactly conserved (Figure 1g5); 3) net charges induced in top metal is zero or a constant depending on its initial state. Figure 1g4 illustrates a whole movement period under sinusoidal excitation: $x(t) = A_F\sin(2\pi ft)$ while the corresponding charge transfer (Q_U) is observed in Figure 1g5. The results show that the phase position of Q_U is out of phase with that of the mechanical shift which is mainly caused by the external resistor and the geometry structure of the MSF-TENG device.

Inevitably charge transfer and redistribution will be affected by the external circuit conditions. Typically, we assume that all charges will be transferred under SC conditions, and **Figure 2**a–c displays the relationship between charge distribution and x/A. When $x/A = -0.83$ (Figure 2c1), total charges in electrode 1 are positive (Figure 2c2) which means that opposite charges are
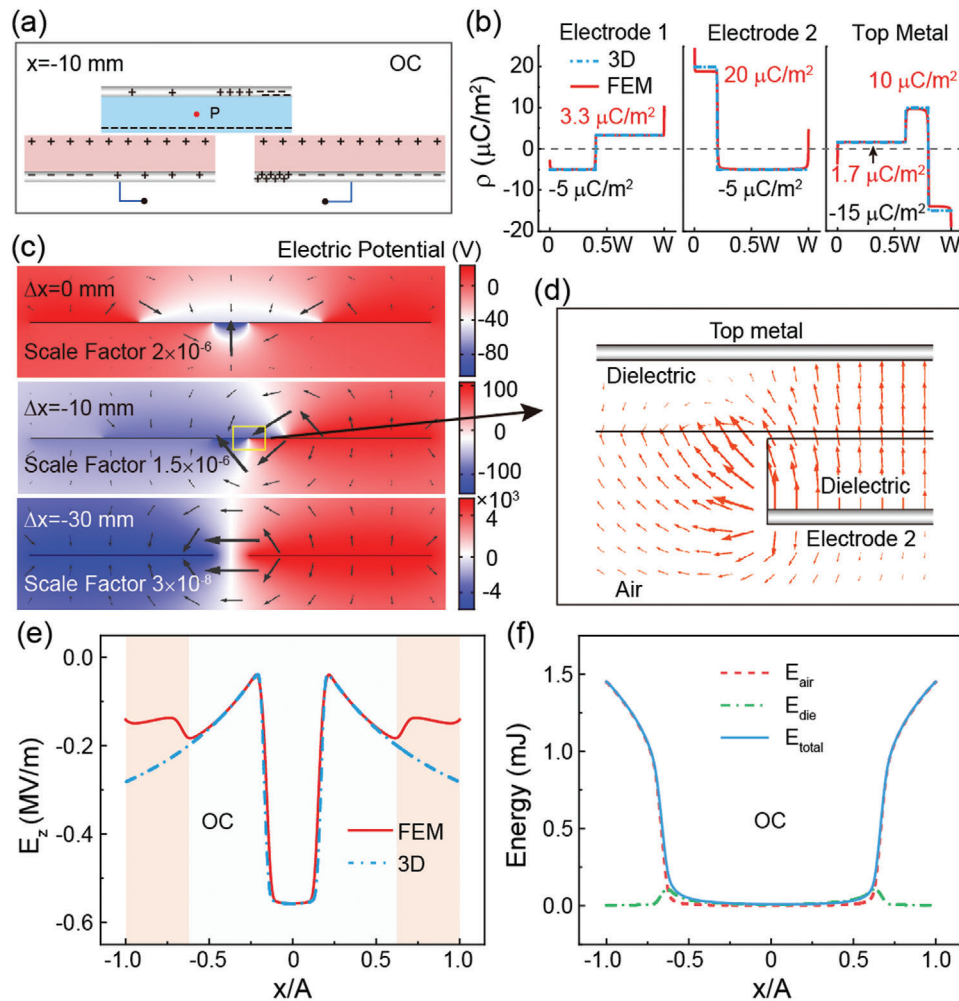
**ADVANCED
SCIENCE NEWS**

www.advancedsciencenews.com

**ADVANCED
PHYSICS
RESEARCH**
Open Access

www.advphysicsres.com

Figure 3. Output characteristics of the MSF-TENG at OC conditions. a) Schematic diagram of the sliding part at $x = -10$ mm, and b) the corresponding charge distributions at electrodes and top metal, respectively. c) Distributions of electric potential and electric field at $x = 0$ mm, -10 mm, and -30 mm, respectively. d) Magnification of electric field at the edge of the dielectric with clearly visible strong edge effects. e) D_z at point P with respect to the ratio x/A. f) Electrostatic energy in the dielectric, air, and the total electrostatic energy of the system at OC conditions.

distributed in electrode 2 (Figure S2, Supporting Information). Although σ at the overlapped regions of the top metal decreases to -0.5 μC m^{-2}, at the non-overlapped regions it is maintained at 10 μC m^{-2} in order to keep the total induced free charge to zero as a consequence of charge conversation. After confirming the free charge distribution, it is necessary to stress the variation of electric displacement (**D**) as x/A changes. Figure 2d demonstrates the change of z-component of **D** (D_z) evaluated at the center of dielectric 1 (the point of P in Figure 2a1). At stage II, D_z keeps a constant (close to -10 μC/m^2) when point P moves within the air gap, but it abruptly increases to 2.5 μC m^{-2} as point P moves into overlapped regions (Figure 2b1). This strange phenomenon is attributed to the free charges changing from positive/negative to negative/positive when the point P moves from the non-overlapped region to the overlapped region. During the sliding process, the small change of D_z indicates that less external energy is needed to change the status of the energy conversion system. However, if x becomes bigger and close to A_F, the corresponding D_z gradually decreases until zero at $x/A = \pm 1$ (Fig-

ure 2c1). From Figure 2e, it is seen that there is little variation of the quasi-electrostatic energy at stage II. On the other hand, if the evaluated point is located at the center of dielectric 2 (Point Q), a sudden change of the corresponding D_z occurs at the overlapped regions (Figure S2, Supporting Information).

The other extreme is that no charge is transferred between the two electrodes at OC conditions (**Figure 3**). The variations of charge distributions are similar to those of a connected external resistor; but the former's performance is highly non-uniform, especially when the overlapped region is rather limited. As illustrated in Figure 3b, when $x = -10$ mm ($x/A = -1/3$), the charge density at the overlapped region of the electrode 2 reaches 20 μC m^{-2}, while in the top metal the charge density suddenly decreases to -15 μC m^{-2} which gives rise to a distortion of the electric field distributed not only in the air gap but also around the edges of dielectrics at the overlapped region (Figure 3c,d). Certainly, the corresponding regions could exhibit an extremely large divergence owing to the non-uniform distribution of free charges in the electrodes. Moreover, the z-component of **E** (E_z) at point P
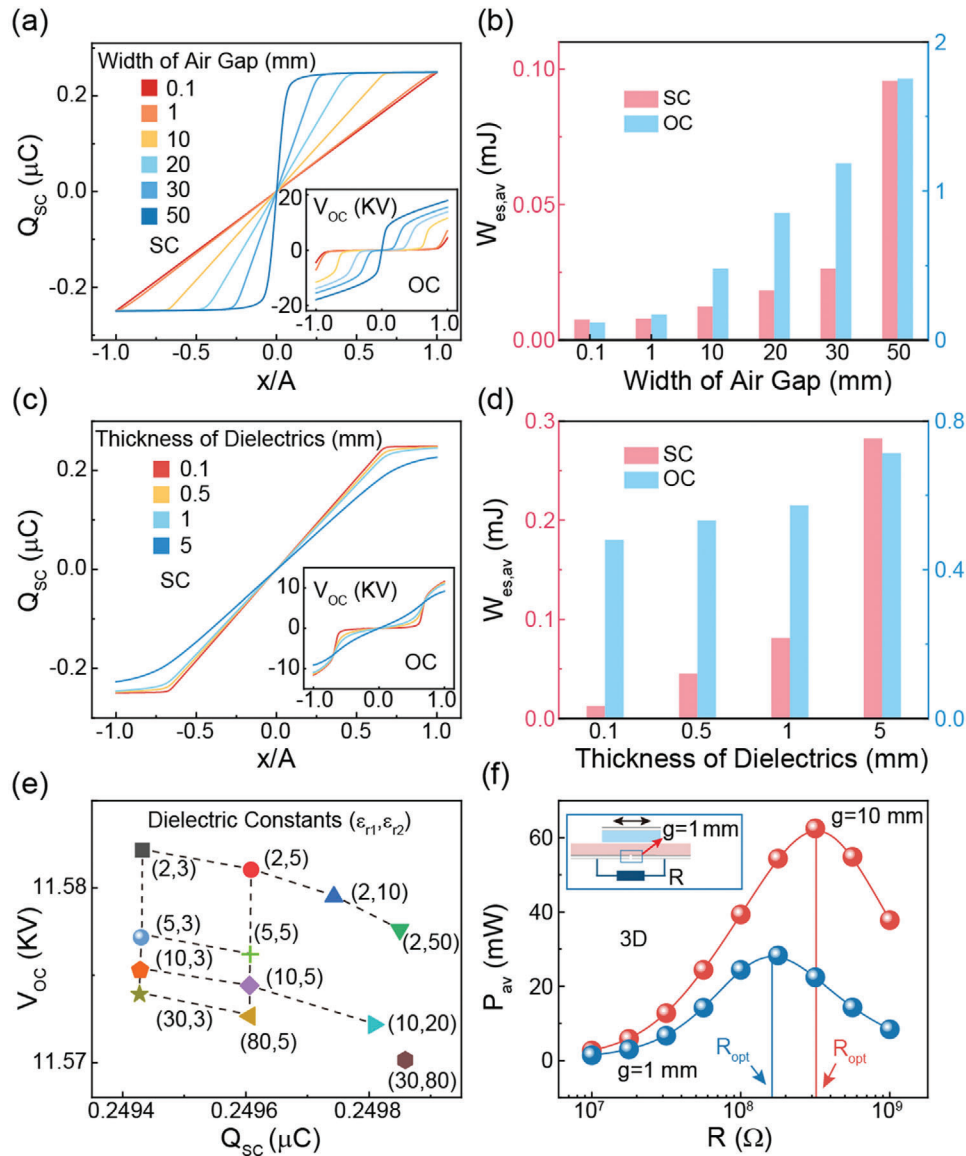
2200039 (6 of 16)

Figure 4. Influence of structural parameters on output characteristics of the MSF-TENG. Influence of the air gap on a) Q_{SC}, V_{OC}, and b) the corresponding average of total electrostatic energy. Influence of the thickness of dielectrics on c) Q_{SC}, V_{OC}, and d) the corresponding average of total electrostatic energy. e) Influence of the permittivity on Q_{SC}, and V_{OC}, respectively. f) P_{av} under various loading conditions for the MSF-TENG when $g = 10$ mm, and $g = 1$ mm (the inset), respectively.

varies as x/A changes (Figure 3e). It is apparent that the strength of E_Z displays a sharp decrease and then changes its direction when the sliding part moves off the central location, indicating that much more energy has been provided to polarize the dielectric 1. As demonstrated in Figure 3f, a large amount of quasi-electrostatic energy (E_{total}) is stored in the MSF-TENG device system, especially when the sliding part moves close to the edge, i.e., $x/A = \pm 1$. Compared to E_{total} and the electrostatic energy distributed in the air (E_{air}), there is nearly no energy distributed in the dielectrics (E_{die}). Evidently, there is no power output to the external circuit under SC or OC conditions; even so, additional mechanical energy should be provided to a TENG energy conversion system so as to change the operation state.

Typically, source quantities and field quantities within the TENGs are usually explored through Maxwell's equations based on a mathematical-physical model while the circuit variables in an external circuit can be revealed by circuit theory according to the capacitive model. Circuit theory is essentially a new abstraction layer created on top of Maxwell's equations which provides convenience for engineering applications, and by which the capacitive model is established. How the design parameters such as the width of air gap between electrodes (g), the thickness of dielectric (d), and dielectric constant (ϵ) influence the basic output performance of the MSF-TENG device has been carried out and demonstrated in **Figure 4**. As g increases, the nonlinear degree of charge transfer becomes more obvious (Figure 4a). This

**ADVANCED
SCIENCE NEWS**

www.advancedsciencenews.com

**ADVANCED
PHYSICS
RESEARCH**
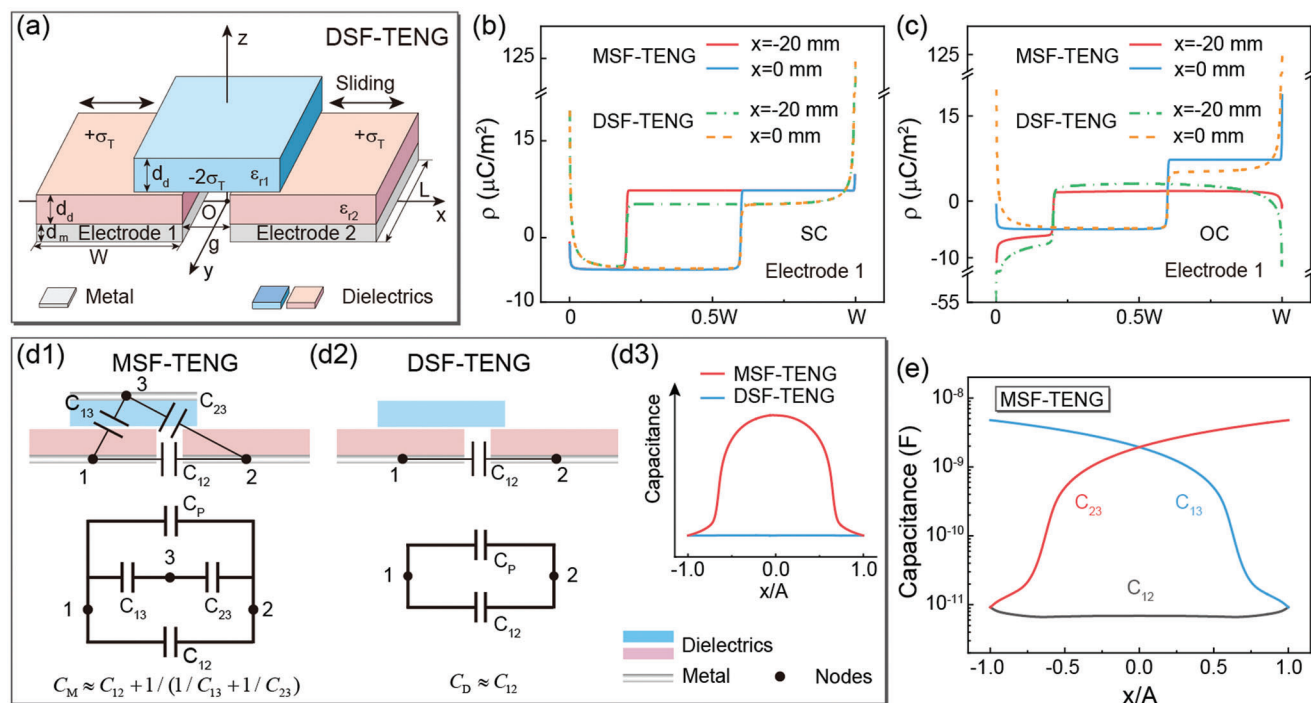
www.advphysicsres.com

Figure 5. Output comparisons of the MSF-TENG and the DSF-TENG. a) Structural schematic diagram of the DSF-TENG. Charge distributions of electrode 1 at b) SC conditions, and c) OC conditions when $x = -20$ mm and $x = 0$ mm, respectively. d) Schematics of equivalent capacitance circuits. e) Individual capacitances of the equivalent capacitance circuit of MSF-TENG with respect to the ratio x/A.

is because the increase of g leads to a decrease in the overlapped regions between dielectric 1 and dielectric 2, resulting in an increased non-uniform charge distribution at the electrodes. However, if the thickness of dielectric is increased, the linear relationship between the thickness and Q_{SC} becomes obvious at different x/A values (Figure 4c). Either increasing g or the thickness of dielectric, the average electrostatic energy ($W_{es,av}$) distributed in the MSF-TENG device exhibits a growing tendency (Figure 4b,d). On the other hand, a larger g will increase the output energy of the MSF-TENG at a fixed frequency, thus affecting the average power (P_{av}) output in the external circuit; yet, it has little effect on the total transferred charges at SC conditions (Q_{SC}). So, the P_{av} is dominated by the peak of V_{OC} ($V_{OC,peak}$) and increases with g (Figure 4f). Except for the thickness of the dielectric, the relative permittivity displays a relatively small effect on V_{OC} and Q_{SC} (Figure 4e). This is because V_{OC} is equivalent to the potential difference between the two electrodes which mainly depends on the charges distributed on them. But it should be noticed that the induced charges on the electrodes of the MSF-TENG are not influenced by the relative permittivity of dielectrics (ϵ_{r1}, ϵ_{r2}). Therefore, although the geometry structure and material selection are important factors, and that affect the output performance, the physical fundament and the relations among variables of a TENG device will never change.

A similar method has been utilized to quantitatively analyze the charge distributions of the DSF-TENG (**Figure 5**a, Note S2, Supporting Information). It can be easily proven that charge distributions of the DSF-TENG are completely similar to those of the MSF-TENG whether at SC or OC conditions (Figure 5b,c). For the MSF-TENG, there are ten different segmented charge

distributions; but the number of segmented charges decreases to seven for the DSF-TENG (Figure S5, Supporting Information). At the overlapped regions, whether under SC or OC conditions, the charge density of the DSF-TENG is lower than that of the MSF-TENG; but at the non-overlapped regions, an opposite effect occurs, in particular at the edges of the electrodes (Figure 5b,c). The biggest reason for this is that the top metal shields the electric field from the external region of TENG device; in other words, this electrostatic shielding will minimize the effects of electric field distortion and the uneven distribution due to space charge. Hence, the electric field distribution of the MSF-TENG should be more uniform when compared with that of the DSF-TENG especially located at the same position (Figure S6, Supporting Information). It is a fact that electrostatic charge-based electric fields diverge away from points of positive charge and converge toward points of negative charge; thus, it is zero if we make a closed-loop integral. This is an important reason why the charge density of the DSF-TENG does not display abrupt changes in the MSF-TENG device. Based on the above assumptions, a comparison of electric flux passing through a closed Gaussian surface of electrode 1 for the DSF-TENG and MSF-TENG is demonstrated in Figure S7 (Supporting Information). The time-variation of electric flux for the MSF-TENG shows obvious non-linear characteristics both at SC conditions and when connected to an optimum resistor which is caused by a sudden change in charge distribution in electrode 1.

Material selection and structure control of a TENG device specify its charge distributions, and then its output characteristics under different mechanical excitations and external electric systems. Equivalent circuit models of the two typical SF-TENGs have
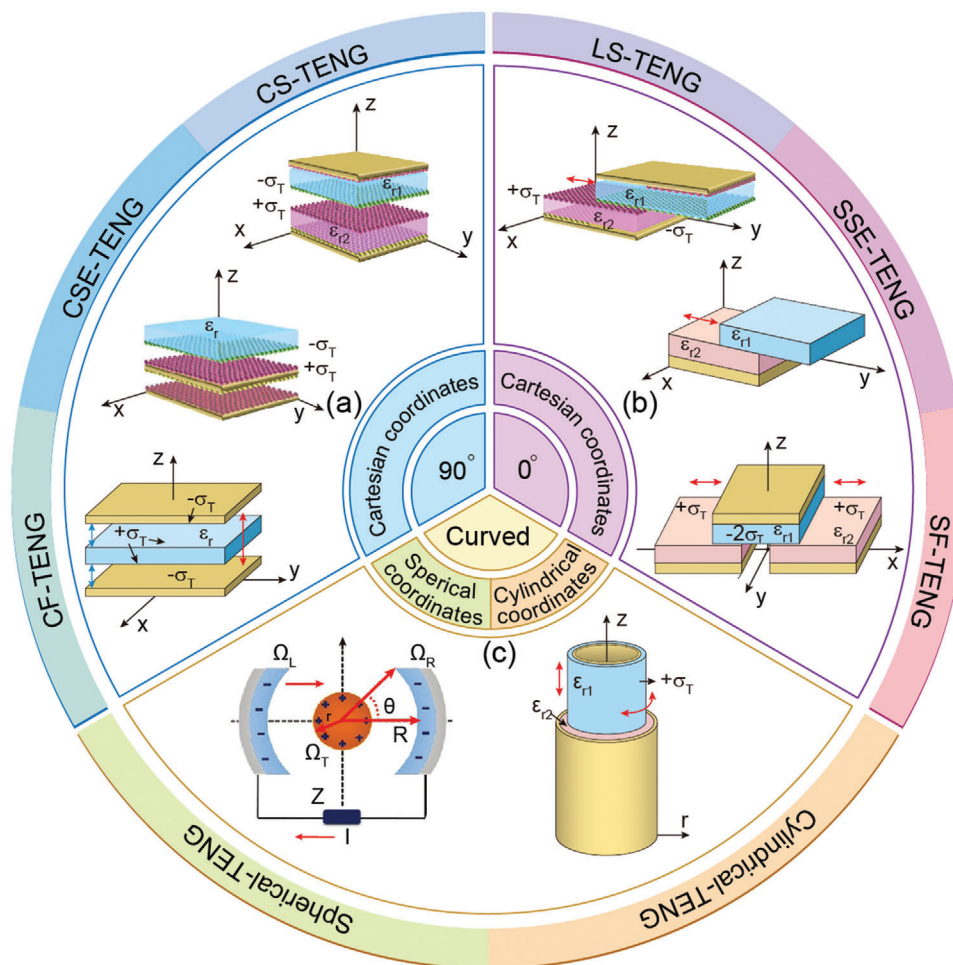
**ADVANCED
SCIENCE NEWS**

www.advancedsciencenews.com

**ADVANCED
PHYSICS
RESEARCH**
Open Access

www.advphysicsres.com

Figure 6. Mathematical-physical model of TENGs with different structures in rectangular coordinates, cylindrical coordinates, and spherical coordinates, respectively. a) The direction of relative movement is parallel to a charged surface, and b) perpendicular to a charged surface, and c) there exists non-planar charge distributions.

been carried out according to the node analysis method that is beneficial to study linear networks (Figure 5d). Because none of the three charged dielectric surfaces are equipotential, they cannot be regarded as three circuit nodes. The capacitance formed between electrodes by tribo-charged surfaces is defined as the parasitic capacitance (C_P) which is usually small and can be neglected. The equivalent capacitance of MSF-TENG (C_M) is written as:

$$C_M = C_{12} + 1/(1/C_{13} + 1/C_{23}) + C_P \approx C_{12} + 1/(1/C_{13} + 1/C_{23})$$

(9)

where C_{12} represents the mutual capacitance between the two electrodes; C_{13}, and C_{23} denote the capacitances between the top metal and electrode 1, top metal and electrode 2, respectively. Using the same approach, the capacitance of DSF-TENG (C_D) is given by:

$$C_D = C_{12} + C_P \approx C_{12}$$

(10)

Numerical results in Figure 5d3 demonstrate that as the sliding part moves side to side, the C_D exhibits little change but an extremely large value for C_M appears when the MSF-TENG is located at the midpoint ($x/A = 0$). Calculated results depicted in Figure 5e show the specific changes of the C_M when x/A varies from -1 to 1, and similar results have been found in previously published work.[32]

The most significant function of a TENG device is that it can convert mechanical energy into electricity; because of this great advantage, it can be utilized either as a power source or a self-powered sensor toward applications. Although different models such as a capacitive model or a mathematical-physical model have been established, they are all based on Maxwell's equations combined with circuit theory. Geometric structure and material selection mainly affect the charge generation and distribution in a TENG device, consequently influencing the displacement current and the external circuit conduction current. In other words, the most important purpose of modeling a TENG is to clarify how the free charges move and redistribute without an external electric field. Therefore, according to the charge distribution and mechanical excitation, the TENGs can be divided into three

ADVANCED
SCIENCE NEWS

www.advancedsciencenews.com

ADVANCED
PHYSICS
RESEARCH
Open Access

www.advphysicsres.com

classes which are illustrated in **Figure 6**: a) the direction of relative movement is parallel to a charged surface, and b) perpendicular to a charged surface, and c) there exists non-planar charge distributions. Combining with different geometry structures, a mathematical-physical model in rectangular coordinates, cylindrical coordinates, spherical coordinates, or other coordinates,[35] is theoretically applicable to any arbitrarily complex charge distributions and different configurations of TENG devices. Moreover, through this model, one can get a full appreciation of the time-varying displacement current which has been proven to be the driving force of TENGs. Note that the above analysis is based on two assumptions: 1) a TENG device is neutral at any time and thus it is equivalent to a lumped element described by a lumped parameter; 2) a TENG device is usually operated under a low working frequency, so it intrinsically relates to the quasi-electromagnetic field distribution. In addition, it is also should be noticed that the edge effect is practically inevitable because the electric field around the edges of TENGs cannot suddenly decrease to zero owing to electrostatics. Therefore, in this work suitable conditions have been chosen to make the influence of edge effect minimum, which is aimed to ensure the above assumptions are always tenable.

4. Conclusion

In summary, we have explored the electricity generation process by a time-varying polarization in the absence of a pre-existing electric field. One of the key points here is to understand the microscopic description caused by variations of free charges distributed on electrodes and contacting surfaces of a TENG device. Unifying the microscopic description with a macroscopic description, it has been proved that the source term P_S (Wang term) is necessarily built into Maxwell's equations because it provides a connection between the microscopic polarization and the associated external energy source, whereby the constitutive relations and the form of Faraday's law, and Maxwell's equations are modified. Different from the traditional electromagnetic generator based on Faraday's law, the electromotive force of a TENG device is a potential difference caused by the free charge distribution which results in a time-variation of the dielectric polarization and subsequently a time-variation of electric displacement (displacement current). This is qualitatively different from the other types of energy harvesting devices.

Moreover, we take the SF-TENG as an example to illustrate the relationship between the free charge distribution and the energy harvesting process. Through a segmented charge distribution, a 3D mathematical-physical model of SF-TENG has been established. We can confirm that the charge distribution and dielectric polarization mainly depend on the geometry structure, material selection, and external circuit conditions. Furthermore, equivalent circuit models of the MSF-TENG and DSF-TENG are present according to lumped parameter circuit theory. Then, we can thoroughly clarify why the total capacitance of the DSF-TENG is almost constant but that of the MSF-TENG is time-varying. Finally, the mathematical-physical model of TENGs in rectangular coordinates, cylindrical coordinates, and spherical coordinates are summarized so as to improve its suitability to a range of geometries. Theoretically, we anticipate that understanding the mechanism of TENGs with any configurations and precisely controlling the dynamic outputs can be accomplished through our approach.

5. Experimental Section

Numerical calculations of the 3D mathematical-physical model are demonstrated through MATLAB software (Mathworks Inc.); and the corresponding modeling process is provided in supplementary Notes S1 and S2. Basic output performances of the SF-TENGs at OC and SC conditions are carried out utilizing COMSOL Multiphysics software with the finite element method (FEM). Parameters utilized in these simulations can be found in Figure S2 (Supporting Information). Note that since the TENG is generally operated at a low working frequency, FEM simulations are performed in a quasi-electrostatic field. When using the software COMSOL, the electric displacement and electric field should satisfy

$$\nabla \cdot \mathbf{D} = \rho_v \qquad (11)$$

$$\mathbf{E} = -\nabla V \qquad (12)$$

where ρ_v and V are the charge density and electric potential related to the spatial position, respectively. The potential of all boundaries of the air domain is set to 0 ($V = 0$). At SC conditions, the electrodes of an SF-TENG are set to have the same floating potential terminal. On the contrary, the floating potentials of each electrode are different at OC conditions. In particular, the floating potential boundary satisfies

$$\int_{\partial\Omega} \mathbf{D} \cdot \mathbf{n} dS = Q_0 \qquad (13)$$

$$V \equiv const \qquad (14)$$

where Ω represents all boundaries of the domains, $\mathbf{n}$ refers to the unit normal vector of the boundary, and Q_0 is the total free charge. Charge densities on the lower surface of dielectric 1 and the upper surfaces of dielectric 2 are set to -10 μC m^{-2}, and 5 μC m^{-2}, respectively. The electric field on both sides of these interfaces between air and dielectric satisfies:

$$(\mathbf{E}_2 - \mathbf{E}_1) \times \mathbf{n} = 0 \qquad (15)$$

$$(\mathbf{D}_2 - \mathbf{D}_1) \cdot \mathbf{n} = \sigma_S \qquad (16)$$

where $\mathbf{E}_1$ ($\mathbf{D}_1$) and $\mathbf{E}_2$ ($\mathbf{D}_2$) represent the electric field (and electric displacement) distributed in air and dielectrics, respectively. $\mathbf{n}$ refers to the unit normal vector of the boundary and σ_S denotes the charge density on the interfaces. All related physical quantities, such as electric charge, electric distribution, electric field, dielectric polarization, and electric displacement can be directly obtained from COMSOL software through post processing. Parameters and materials of simulations using COMSOL software for the MSF-TENG and DSF-TENG device which are listed in **Table 1**.

Appendix A: Charge distribution of MSF-TENG

Table A1.

State I: $W_{10} = x_2(t)-x_1$, $W_{11} = x_3-x_2(t)$, $W_{20} = W$, $W_{21} = 0$;

State II: $W_{10} = x_2(t)-x_1$, $W_{11} = x_3-x_2(t)$, $W_{20} = x_6-x_5(t)$, $W_{21} = x_5(t)-x_4$;

State III: $W_{10} = W$, $W_{11} = 0$, $W_{20} = x_6-x_5(t)$, $W_{21} = x_5(t)-x_4$.

**ADVANCED
SCIENCE NEWS**

www.advancedsciencenews.com

**ADVANCED
PHYSICS
RESEARCH**
Open Access

www.advphysicsres.com

Table A1. Charge density on charged surfaces for the three spatial states of the MSF-TENG.

Surface	State I (Figure 1d)	State II (Figure 1e)	State III (Figure 1f)
1	$-2\sigma_T$	$-2\sigma_T$	$-2\sigma_T$
2	σ_T	σ_T	σ_T
3	σ_T	σ_T	σ_T
4	$-\sigma_T$	$-\sigma_T$	$-\sigma_T$
5	$-Q_U/W_{11}+\sigma_T W_{10}/W_{11}$	$-\sigma_T$	$Q_U/W_{21}+\sigma_T W_{20}/W_{21}$
6	Q_U/W_{20}	$-Q_U/W_{11}+\sigma_T W_{10}/W_{11}$	$-Q_U/W_{10}$
7	$\sigma_T-\sigma_T W_{10}/W_{11}+Q_U/W_{11}$	$Q_U/W_{21}+\sigma_T W_{20}/W_{21}$	$\sigma_T-\sigma_T W_{20}/W_{21}-Q_U/W_{21}$
8	$-W_{11}(\sigma_T-\sigma_T W_{10}/W_{11}+Q_U/W_{11})/W_{10}$	$2\sigma_T$	$-W_{21}(\sigma_T-\sigma_T W_{20}/W_{21}-Q_U/W_{21})/W_{20}$
9	–	$\sigma_T-\sigma_T W_{10}/W_{11}+Q_U/W_{11}$	–
10	–	$\sigma_T-\sigma_T W_{20}/W_{21}-Q_U/W_{21}$	–

Note: W_{10} and W_{11} represent the width of the non-overlapping portion and the overlapping portion of electrode 1 and the freestanding layer, respectively. W_{20} and W_{21} represents the width of the non-overlapping portion and the overlapping portion of electrode 2 and the freestanding layer, respectively. Q_U stands for the transferred charges between electrodes.

Appendix B: Electric potential of MSF-TENG

When the freestanding layer is located in state I, the electric potential of electrode 1 can be calculated by:

$$\phi_1(t) = \sum_{i=1}^{8} \phi_{i,1}(t) \tag{B1}$$

where

$$\phi_{1,1}(t) = \frac{-2\sigma_T}{4\pi\varepsilon_0} \left\{ \int_{x_3}^{x_5(t)} \int_{-\frac{L}{2}}^{\frac{L}{2}} \frac{dx'\,dy'}{\left[(x_A-x')^2+(y_A-y')^2+(z_A-z_1)^2\right]^{1/2}} + \int_{x_2(t)}^{x_3} \int_{-\frac{L}{2}}^{\frac{L}{2}} \frac{dx'\,dy'}{\left[(x_C-x')^2+(y_C-y')^2+(z_C-z_1)^2\right]^{1/2}} \right\} \tag{B1.1}$$

$$\phi_{2,1}(t) = \frac{\sigma_T}{4\pi\varepsilon_0} \left\{ \int_{x_1}^{x_2(t)} \int_{-\frac{L}{2}}^{\frac{L}{2}} \frac{dx'\,dy'}{\left[(x_B-x')^2+(y_B-y')^2+(z_B-z_2)^2\right]^{1/2}} + \int_{x_2(t)}^{x_3} \int_{-\frac{L}{2}}^{\frac{L}{2}} \frac{dx'\,dy'}{\left[(x_C-x')^2+(y_C-y')^2+(z_C-z_2)^2\right]^{1/2}} \right\} \tag{B1.2}$$

$$\phi_{3,1}(t) = \frac{\sigma_T}{4\pi\varepsilon_0} \int_{x_4}^{x_6} \int_{-\frac{L}{2}}^{\frac{L}{2}} \frac{dx'\,dy'}{\left[(x_A-x')^2+(y_A-y')^2+(z_A-z_3)^2\right]^{1/2}} \tag{B1.3}$$

$$\phi_{4,1}(t) = \frac{-\sigma_T}{4\pi\varepsilon_0} \int_{x_1}^{x_2(t)} \int_{-\frac{L}{2}}^{\frac{L}{2}} \frac{dx'\,dy'}{\left[(x_B-x')^2+(y_B-y')^2+(z_B-z_4)^2\right]^{1/2}} \tag{B1.4}$$

$$\phi_{5,1}(t) = \frac{1}{4\pi\varepsilon_0} \left(-\frac{Q_U}{W_{11}} + \frac{\sigma_T W_{10}}{W_{11}} \right) \int_{x_2(t)}^{x_3} \int_{-\frac{L}{2}}^{\frac{L}{2}} \frac{dx'\,dy'}{\left[(x_C-x')^2+(y_C-y')^2+(z_C-z_5)^2\right]^{1/2}} \tag{B1.5}$$

$$\phi_{6,1}(t) = \frac{Q_U}{4\pi\varepsilon_0 W_{20}} \int_{x_4}^{x_6} \int_{-\frac{L}{2}}^{\frac{L}{2}} \frac{dx'\,dy'}{\left[(x_A-x')^2+(y_A-y')^2+(z_A-z_6)^2\right]^{1/2}} \tag{B1.6}$$

$$\phi_{7,1}(t) = \frac{1}{4\pi\varepsilon_0} \left(\sigma_T - \frac{\sigma_T W_{10}}{W_{11}} + \frac{Q_U}{W_{11}} \right) \int_{x_2(t)}^{x_3} \int_{-\frac{L}{2}}^{\frac{L}{2}} \frac{dx'\,dy'}{\left[(x_C-x')^2+(y_C-y')^2+(z_C-z_7)^2\right]^{1/2}} \tag{B1.7}$$

$$\phi_{8,1}(t) = -\frac{W_{11}}{4\pi\varepsilon_0 W_{10}} \left(\sigma_T - \frac{\sigma_T W_{10}}{W_{11}} + \frac{Q_U}{W_{11}} \right) \int_{x_3}^{x_5(t)} \int_{-\frac{L}{2}}^{\frac{L}{2}} \frac{dx'dy'}{\left[(x_A - x')^2 + (y_A - y')^2 + (z_A - z_8)^2 \right]^{1/2}} \tag{B1.8}$$

In the same way, the electric potential of electrode 2 can be obtained:

$$\phi_2(t) = \sum_{i=1}^{8} \phi_{i,2}(t) \tag{B2}$$

where

$$\phi_{1,2}(t) = \frac{-2\sigma_T}{4\pi\varepsilon_0} \int_{x_2(t)}^{x_5(t)} \int_{-\frac{L}{2}}^{\frac{L}{2}} \frac{dx'dy'}{\left[(x_D - x')^2 + (y_D - y')^2 + (z_D - z_1)^2 \right]^{1/2}} \tag{B2.1}$$

$$\phi_{2,2}(t) = \frac{\sigma_T}{4\pi\varepsilon_0} \int_{x_1}^{x_3} \int_{-\frac{L}{2}}^{\frac{L}{2}} \frac{dx'dy'}{\left[(x_D - x')^2 + (y_D - y')^2 + (z_D - z_2)^2 \right]^{1/2}} \tag{B2.2}$$

$$\phi_{3,2}(t) = \frac{\sigma_T}{4\pi\varepsilon_0} \int_{x_4}^{x_6} \int_{-\frac{L}{2}}^{\frac{L}{2}} \frac{dx'dy'}{\left[(x_D - x')^2 + (y_D - y')^2 + (z_D - z_3)^2 \right]^{1/2}} \tag{B2.3}$$

$$\phi_{4,2}(t) = \frac{-\sigma_T}{4\pi\varepsilon_0} \int_{x_1}^{x_2(t)} \int_{-\frac{L}{2}}^{\frac{L}{2}} \frac{dx'dy'}{\left[(x_D - x')^2 + (y_D - y')^2 + (z_D - z_4)^2 \right]^{1/2}} \tag{B2.4}$$

$$\phi_{5,2}(t) = \frac{1}{4\pi\varepsilon_0} \left(-\frac{Q_U}{W_{11}} + \frac{\sigma_T W_{10}}{W_{11}} \right) \int_{x_2(t)}^{x_3} \int_{-\frac{L}{2}}^{\frac{L}{2}} \frac{dx'dy'}{\left[(x_D - x')^2 + (y_D - y')^2 + (z_D - z_5)^2 \right]^{1/2}} \tag{B2.5}$$

$$\phi_{6,2}(t) = \frac{Q_U}{4\pi\varepsilon_0 W_{20}} \int_{x_4}^{x_6} \int_{-\frac{L}{2}}^{\frac{L}{2}} \frac{dx'dy'}{\left[(x_D - x')^2 + (y_D - y')^2 + (z_D - z_6)^2 \right]^{1/2}} \tag{B2.6}$$

$$\phi_{7,2}(t) = \frac{1}{4\pi\varepsilon_0} \left(\sigma_T - \frac{\sigma_T W_{10}}{W_{11}} + \frac{Q_U}{W_{11}} \right) \int_{x_2(t)}^{x_3} \int_{-\frac{L}{2}}^{\frac{L}{2}} \frac{dx'dy'}{\left[(x_D - x')^2 + (y_D - y')^2 + (z_D - z_7)^2 \right]^{1/2}} \tag{B2.7}$$

$$\phi_{8,2}(t) = -\frac{W_{11}}{4\pi\varepsilon_0 W_{10}} \left(\sigma_T - \frac{\sigma_T W_{10}}{W_{11}} + \frac{Q_U}{W_{11}} \right) \int_{x_3}^{x_5(t)} \int_{-\frac{L}{2}}^{\frac{L}{2}} \frac{dx'dy'}{\left[(x_D - x')^2 + (y_D - y')^2 + (z_D - z_8)^2 \right]^{1/2}} \tag{B2.8}$$

For Equation (B1.1) – (B2.8), the coordinate of points A–D in Figure 1d is represented by $(x_\alpha, y_\alpha, z_\alpha)$, where α denotes these capital letters, respectively. z_i (where i takes the value from 1 to 8) represents the z-positions of these different eight charged planes, respectively; in particular, we have $z_2 = z_3, z_4 = z_5 = z_6, z_7 = z_8$.

When the freestanding layer is in state II, the electric potential of electrode 1 can be calculated by:

$$\phi_1(t) = \sum_{i=1}^{10} \phi_{i,1}(t) \tag{B3}$$

where

$$\phi_{1,1}(t) = \frac{-2\sigma_T}{4\pi\varepsilon_0} \left\{ \int_{x_3}^{x_5(t)} \int_{-\frac{L}{2}}^{\frac{L}{2}} \frac{dx'dy'}{\left[(x_A - x')^2 + (y_A - y')^2 + (z_A - z_1)^2 \right]^{1/2}} + \int_{x_2(t)}^{x_3} \int_{-\frac{L}{2}}^{\frac{L}{2}} \frac{dx'dy'}{\left[(x_C - x')^2 + (y_C - y')^2 + (z_C - z_1)^2 \right]^{1/2}} \right\} \tag{B3.1}$$

$$\phi_{2,1}(t) = \frac{\sigma_\mathrm{T}}{4\pi\varepsilon_0}\left\{\int_{x_1}^{x_2(t)}\int_{-\frac{L}{2}}^{\frac{L}{2}}\frac{dx'\,dy'}{\left[(x_\mathrm{B}-x')^2+(y_\mathrm{B}-y')^2+(z_\mathrm{B}-z_2)^2\right]^{1/2}} + \int_{x_2(t)}^{x_3}\int_{-\frac{L}{2}}^{\frac{L}{2}}\frac{dx'\,dy'}{\left[(x_\mathrm{C}-x')^2+(y_\mathrm{C}-y')^2+(z_\mathrm{C}-z_2)^2\right]^{1/2}}\right\} \quad \text{(B3.2)}$$

$$\phi_{3,1}(t) = \frac{\sigma_\mathrm{T}}{4\pi\varepsilon_0}\int_{x_4}^{x_6}\int_{-\frac{L}{2}}^{\frac{L}{2}}\frac{dx'\,dy'}{\left[(x_\mathrm{A}-x')^2+(y_\mathrm{A}-y')^2+(z_\mathrm{A}-z_3)^2\right]^{1/2}} \quad \text{(B3.3)}$$

$$\phi_{4,1}(t) = \frac{-\sigma_\mathrm{T}}{4\pi\varepsilon_0}\int_{x_1}^{x_2(t)}\int_{-\frac{L}{2}}^{\frac{L}{2}}\frac{dx'\,dy'}{\left[(x_\mathrm{B}-x')^2+(y_\mathrm{B}-y')^2+(z_\mathrm{B}-z_4)^2\right]^{1/2}} \quad \text{(B3.4)}$$

$$\phi_{5,1}(t) = \frac{-\sigma_\mathrm{T}}{4\pi\varepsilon_0}\int_{x_5(t)}^{x_6}\int_{-\frac{L}{2}}^{\frac{L}{2}}\frac{dx'\,dy'}{\left[(x_\mathrm{A}-x')^2+(y_\mathrm{A}-y')^2+(z_\mathrm{A}-z_5)^2\right]^{1/2}} \quad \text{(B3.5)}$$

$$\phi_{6,1}(t) = \frac{1}{4\pi\varepsilon_0}\left(-\frac{Q_\mathrm{U}}{W_{11}}+\frac{\sigma_\mathrm{T}W_{10}}{W_{11}}\right)\int_{x_2(t)}^{x_3}\int_{-\frac{L}{2}}^{\frac{L}{2}}\frac{dx'\,dy'}{\left[(x_\mathrm{C}-x')^2+(y_\mathrm{C}-y')^2+(z_\mathrm{C}-z_6)^2\right]^{1/2}} \quad \text{(B3.6)}$$

$$\phi_{7,1}(t) = \frac{1}{4\pi\varepsilon_0}\left(\frac{Q_\mathrm{U}}{W_{21}}+\frac{\sigma_\mathrm{T}W_{20}}{W_{21}}\right)\int_{x_4}^{x_5(t)}\int_{-\frac{L}{2}}^{\frac{L}{2}}\frac{dx'\,dy'}{\left[(x_\mathrm{A}-x')^2+(y_\mathrm{A}-y')^2+(z_\mathrm{A}-z_7)^2\right]^{1/2}} \quad \text{(B3.7)}$$

$$\phi_{8,1}(t) = \frac{2\sigma_\mathrm{T}}{4\pi\varepsilon_0}\int_{x_3}^{x_4}\int_{-\frac{L}{2}}^{\frac{L}{2}}\frac{dx'\,dy'}{\left[(x_\mathrm{A}-x')^2+(y_\mathrm{A}-y')^2+(z_\mathrm{A}-z_8)^2\right]^{1/2}} \quad \text{(B3.8)}$$

$$\phi_{9,1}(t) = \frac{1}{4\pi\varepsilon_0}\left(\sigma_\mathrm{T}-\frac{\sigma_\mathrm{T}W_{10}}{W_{11}}+\frac{Q_\mathrm{U}}{W_{11}}\right)\int_{x_2(t)}^{x_3}\int_{-\frac{L}{2}}^{\frac{L}{2}}\frac{dx'\,dy'}{\left[(x_\mathrm{C}-x')^2+(y_\mathrm{C}-y')^2+(z_\mathrm{C}-z_9)^2\right]^{1/2}} \quad \text{(B3.9)}$$

$$\phi_{10,1}(t) = \frac{1}{4\pi\varepsilon_0}\left(\sigma_\mathrm{T}-\frac{\sigma_\mathrm{T}W_{20}}{W_{21}}-\frac{Q_\mathrm{U}}{W_{21}}\right)\int_{x_4}^{x_5(t)}\int_{-\frac{L}{2}}^{\frac{L}{2}}\frac{dx'\,dy'}{\left[(x_\mathrm{A}-x')^2+(y_\mathrm{A}-y')^2+(z_\mathrm{A}-z_{10})^2\right]^{1/2}} \quad \text{(B3.10)}$$

The electric potential of electrode 2 is given by:

$$\phi_2(t) = \sum_{i=1}^{10}\phi_{i,2}(t) \quad \text{(B4)}$$

where

$$\phi_{1,2}(t) = \frac{-2\sigma_\mathrm{T}}{4\pi\varepsilon_0}\left\{\int_{x_2(t)}^{x_4}\int_{-\frac{L}{2}}^{\frac{L}{2}}\frac{dx'\,dy'}{\left[(x_\mathrm{D}-x')^2+(y_\mathrm{D}-y')^2+(z_\mathrm{D}-z_1)^2\right]^{1/2}} + \int_{x_4}^{x_5(t)}\int_{-\frac{L}{2}}^{\frac{L}{2}}\frac{dx'\,dy'}{\left[(x_\mathrm{F}-x')^2+(y_\mathrm{F}-y')^2+(z_\mathrm{F}-z_1)^2\right]^{1/2}}\right\} \quad \text{(B4.1)}$$

$$\phi_{2,2}(t) = \frac{\sigma_\mathrm{T}}{4\pi\varepsilon_0}\int_{x_1}^{x_3}\int_{-\frac{L}{2}}^{\frac{L}{2}}\frac{dx'\,dy'}{\left[(x_\mathrm{D}-x')^2+(y_\mathrm{D}-y')^2+(z_\mathrm{D}-z_2)^2\right]^{1/2}} \quad \text{(B4.2)}$$

$$\phi_{3,2}(t) = \frac{\sigma_\mathrm{T}}{4\pi\varepsilon_0}\left\{\int_{x_4}^{x_5(t)}\int_{-\frac{L}{2}}^{\frac{L}{2}}\frac{dx'\,dy'}{\left[(x_\mathrm{F}-x')^2+(y_\mathrm{F}-y')^2+(z_\mathrm{F}-z_3)^2\right]^{1/2}} + \int_{x_5(t)}^{x_6}\int_{-\frac{L}{2}}^{\frac{L}{2}}\frac{dx'\,dy'}{\left[(x_\mathrm{E}-x')^2+(y_\mathrm{E}-y')^2+(z_\mathrm{E}-z_3)^2\right]^{1/2}}\right\} \quad \text{(B4.3)}$$

**ADVANCED
SCIENCE NEWS**

www.advancedsciencenews.com

**ADVANCED
PHYSICS
RESEARCH**

www.advphysicsres.com

$$\phi_{4,2}(t) = \frac{-\sigma_{\mathrm{T}}}{4\pi\varepsilon_0} \int_{x_1}^{x_2(t)} \int_{-\frac{L}{2}}^{\frac{L}{2}} \frac{dx'\,dy'}{\left[(x_{\mathrm{D}} - x')^2 + (y_{\mathrm{D}} - y')^2 + (z_{\mathrm{D}} - z_4)^2 \right]^{1/2}} \tag{B4.4}$$

$$\phi_{5,2}(t) = \frac{-\sigma_{\mathrm{T}}}{4\pi\varepsilon_0} \int_{x_5(t)}^{x_6} \int_{-\frac{L}{2}}^{\frac{L}{2}} \frac{dx'\,dy'}{\left[(x_{\mathrm{E}} - x')^2 + (y_{\mathrm{E}} - y')^2 + (z_{\mathrm{E}} - z_5)^2 \right]^{1/2}} \tag{B4.5}$$

$$\phi_{6,2}(t) = \frac{1}{4\pi\varepsilon_0} \left(-\frac{Q_{\mathrm{U}}}{W_{11}} + \frac{\sigma_{\mathrm{T}} W_{10}}{W_{11}} \right) \int_{x_2(t)}^{x_3} \int_{-\frac{L}{2}}^{\frac{L}{2}} \frac{dx'\,dy'}{\left[(x_{\mathrm{D}} - x')^2 + (y_{\mathrm{D}} - y')^2 + (z_{\mathrm{D}} - z_6)^2 \right]^{1/2}} \tag{B4.6}$$

$$\phi_{7,2}(t) = \frac{1}{4\pi\varepsilon_0} \left(\frac{Q_{\mathrm{U}}}{W_{21}} + \frac{\sigma_{\mathrm{T}} W_{20}}{W_{21}} \right) \int_{x_4}^{x_5(t)} \int_{-\frac{L}{2}}^{\frac{L}{2}} \frac{dx'\,dy'}{\left[(x_{\mathrm{F}} - x')^2 + (y_{\mathrm{F}} - y')^2 + (z_{\mathrm{F}} - z_7)^2 \right]^{1/2}} \tag{B4.7}$$

$$\phi_{8,2}(t) = \frac{2\sigma_{\mathrm{T}}}{4\pi\varepsilon_0} \int_{x_3}^{x_4} \int_{-\frac{L}{2}}^{\frac{L}{2}} \frac{dx'\,dy'}{\left[(x_{\mathrm{D}} - x')^2 + (y_{\mathrm{D}} - y')^2 + (z_{\mathrm{D}} - z_8)^2 \right]^{1/2}} \tag{B4.8}$$

$$\phi_{9,2}(t) = \frac{1}{4\pi\varepsilon_0} \left(\sigma_{\mathrm{T}} - \frac{\sigma_{\mathrm{T}} W_{10}}{W_{11}} + \frac{Q_{\mathrm{U}}}{W_{11}} \right) \int_{x_2(t)}^{x_3} \int_{-\frac{L}{2}}^{\frac{L}{2}} \frac{dx'\,dy'}{\left[(x_{\mathrm{D}} - x')^2 + (y_{\mathrm{D}} - y')^2 + (z_{\mathrm{D}} - z_9)^2 \right]^{1/2}} \tag{B4.9}$$

$$\phi_{10,2}(t) = \frac{1}{4\pi\varepsilon_0} \left(\sigma_{\mathrm{T}} - \frac{\sigma_{\mathrm{T}} W_{20}}{W_{21}} - \frac{Q_{\mathrm{U}}}{W_{21}} \right) \int_{x_4}^{x_5(t)} \int_{-\frac{L}{2}}^{\frac{L}{2}} \frac{dx'\,dy'}{\left[(x_{\mathrm{F}} - x')^2 + (y_{\mathrm{F}} - y')^2 + (z_{\mathrm{F}} - z_{10})^2 \right]^{1/2}} \tag{B4.10}$$

For Equation (B3.1) – (B4.10), the coordinate of points A–F in Figure 1e is represented by $(x_\alpha, y_\alpha, z_\alpha)$, where α denotes these capital letters, respectively. z_i (where i takes the value from 1 to 10) represents the z-positions of these different ten charged planes, respectively; in particular, we have $z_2 = z_3$, $z_4 = z_5 = z_6 = z_7$, $z_8 = z_9 = z_{10}$.

When the freestanding layer is in state III, the electric potential of electrode 1 can be obtained:

$$\phi_1(t) = \sum_{i=1}^{8} \phi_{i,1}(t) \tag{B5}$$

where

$$\phi_{1,1}(t) = \frac{-2\sigma_{\mathrm{T}}}{4\pi\varepsilon_0} \int_{x_2(t)}^{x_5(t)} \int_{-\frac{L}{2}}^{\frac{L}{2}} \frac{dx'\,dy'}{\left[(x_{\mathrm{A}} - x')^2 + (y_{\mathrm{A}} - y')^2 + (z_{\mathrm{A}} - z_1)^2 \right]^{1/2}} \tag{B5.1}$$

$$\phi_{2,1}(t) = \frac{\sigma_{\mathrm{T}}}{4\pi\varepsilon_0} \int_{x_1}^{x_3} \int_{-\frac{L}{2}}^{\frac{L}{2}} \frac{dx'\,dy'}{\left[(x_{\mathrm{A}} - x')^2 + (y_{\mathrm{A}} - y')^2 + (z_{\mathrm{A}} - z_2)^2 \right]^{1/2}} \tag{B5.2}$$

$$\phi_{3,1}(t) = \frac{\sigma_{\mathrm{T}}}{4\pi\varepsilon_0} \int_{x_4}^{x_6} \int_{-\frac{L}{2}}^{\frac{L}{2}} \frac{dx'\,dy'}{\left[(x_{\mathrm{A}} - x')^2 + (y_{\mathrm{A}} - y')^2 + (z_{\mathrm{A}} - z_3)^2 \right]^{1/2}} \tag{B5.3}$$

$$\phi_{4,1}(t) = \frac{-\sigma_{\mathrm{T}}}{4\pi\varepsilon_0} \int_{x_5(t)}^{x_6} \int_{-\frac{L}{2}}^{\frac{L}{2}} \frac{dx'\,dy'}{\left[(x_{\mathrm{A}} - x')^2 + (y_{\mathrm{A}} - y')^2 + (z_{\mathrm{A}} - z_4)^2 \right]^{1/2}} \tag{B5.4}$$

$$\phi_{5,1}(t) = \frac{1}{4\pi\varepsilon_0} \left(\frac{Q_{\mathrm{U}}}{W_{21}} + \frac{\sigma_{\mathrm{T}} W_{20}}{W_{21}} \right) \int_{x_4}^{x_5(t)} \int_{-\frac{L}{2}}^{\frac{L}{2}} \frac{dx'\,dy'}{\left[(x_{\mathrm{A}} - x')^2 + (y_{\mathrm{A}} - y')^2 + (z_{\mathrm{A}} - z_5)^2 \right]^{1/2}} \tag{B5.5}$$

$$\phi_{6,1}(t) = -\frac{Q_U}{4\pi\varepsilon_0 W_{10}} \int_{x_1}^{x_3} \int_{-\frac{L}{2}}^{\frac{L}{2}} \frac{dx' dy'}{\left[(x_A - x')^2 + (y_A - y')^2 + (z_A - z_6)^2 \right]^{1/2}} \tag{B5.6}$$

$$\phi_{7,1}(t) = \frac{1}{4\pi\varepsilon_0} \left(\sigma_T - \frac{\sigma_T W_{20}}{W_{21}} - \frac{Q_U}{W_{21}} \right) \int_{x_4}^{x_5(t)} \int_{-\frac{L}{2}}^{\frac{L}{2}} \frac{dx' dy'}{\left[(x_A - x')^2 + (y_A - y')^2 + (z_A - z_7)^2 \right]^{1/2}} \tag{B5.7}$$

$$\phi_{8,1}(t) = -\frac{W_{21}}{4\pi\varepsilon_0 W_{20}} \left(\sigma_T - \frac{\sigma_T W_{20}}{W_{21}} - \frac{Q_U}{W_{21}} \right) \int_{x_2(t)}^{x_4} \int_{-\frac{L}{2}}^{\frac{L}{2}} \frac{dx' dy'}{\left[(x_A - x')^2 + (y_A - y')^2 + (z_A - z_8)^2 \right]^{1/2}} \tag{B5.8}$$

The electric potential of electrode 2 is:

$$\phi_2(t) = \sum_{i=1}^{8} \phi_{i,2}(t) \tag{B6}$$

where

$$\phi_{1,2}(t) = \frac{-2\sigma_T}{4\pi\varepsilon_0} \left\{ \int_{x_2(t)}^{x_4} \int_{-\frac{L}{2}}^{\frac{L}{2}} \frac{dx' dy'}{\left[(x_D - x')^2 + (y_D - y')^2 + (z_D - z_1)^2 \right]^{1/2}} + \int_{x_4}^{x_5(t)} \int_{-\frac{L}{2}}^{\frac{L}{2}} \frac{dx' dy'}{\left[(x_F - x')^2 + (y_F - y')^2 + (z_F - z_1)^2 \right]^{1/2}} \right\} \tag{B6.1}$$

$$\phi_{2,2}(t) = \frac{\sigma_T}{4\pi\varepsilon_0} \int_{x_1}^{x_3} \int_{-\frac{L}{2}}^{\frac{L}{2}} \frac{dx' dy'}{\left[(x_D - x')^2 + (y_D - y')^2 + (z_D - z_2)^2 \right]^{1/2}} \tag{B6.2}$$

$$\phi_{3,2}(t) = \frac{\sigma_T}{4\pi\varepsilon_0} \left\{ \int_{x_4}^{x_5(t)} \int_{-\frac{L}{2}}^{\frac{L}{2}} \frac{dx' dy'}{\left[(x_F - x')^2 + (y_F - y')^2 + (z_F - z_3)^2 \right]^{1/2}} + \int_{x_5(t)}^{x_6} \int_{-\frac{L}{2}}^{\frac{L}{2}} \frac{dx' dy'}{\left[(x_E - x')^2 + (y_E - y')^2 + (z_E - z_3)^2 \right]^{1/2}} \right\} \tag{B6.3}$$

$$\phi_{4,2}(t) = \frac{-\sigma_T}{4\pi\varepsilon_0} \int_{x_5(t)}^{x_6} \int_{-\frac{L}{2}}^{\frac{L}{2}} \frac{dx' dy'}{\left[(x_E - x')^2 + (y_E - y')^2 + (z_E - z_4)^2 \right]^{1/2}} \tag{B6.4}$$

$$\phi_{5,2}(t) = \frac{1}{4\pi\varepsilon_0} \left(\frac{Q_U}{W_{21}} + \frac{\sigma_T W_{20}}{W_{21}} \right) \int_{x_4}^{x_5(t)} \int_{-\frac{L}{2}}^{\frac{L}{2}} \frac{dx' dy'}{\left[(x_F - x')^2 + (y_F - y')^2 + (z_F - z_5)^2 \right]^{1/2}} \tag{B6.5}$$

$$\phi_{6,2}(t) = -\frac{Q_U}{4\pi\varepsilon_0 W_{10}} \int_{x_1}^{x_3} \int_{-\frac{L}{2}}^{\frac{L}{2}} \frac{dx' dy'}{\left[(x_D - x')^2 + (y_D - y')^2 + (z_D - z_6)^2 \right]^{1/2}} \tag{B6.6}$$

$$\phi_{7,2}(t) = \frac{1}{4\pi\varepsilon_0} \left(\sigma_T - \frac{\sigma_T W_{20}}{W_{21}} - \frac{Q_U}{W_{21}} \right) \int_{x_4}^{x_5(t)} \int_{-\frac{L}{2}}^{\frac{L}{2}} \frac{dx' dy'}{\left[(x_F - x')^2 + (y_F - y')^2 + (z_F - z_7)^2 \right]^{1/2}} \tag{B6.7}$$

$$\phi_{8,2}(t) = -\frac{W_{21}}{4\pi\varepsilon_0 W_{20}} \left(\sigma_T - \frac{\sigma_T W_{20}}{W_{21}} - \frac{Q_U}{W_{21}} \right) \int_{x_2(t)}^{x_4} \int_{-\frac{L}{2}}^{\frac{L}{2}} \frac{dx' dy'}{\left[(x_D - x')^2 + (y_D - y')^2 + (z_D - z_8)^2 \right]^{1/2}} \tag{B6.8}$$

For Equation (B5.1) – (B6.8), the coordinates of points A and D–F in Figure 1f are represented by $(x_\alpha, y_\alpha, z_\alpha)$, where α denotes these capital letters, respectively. z_i (where i takes the value from 1 to 8) represents the z-positions of these different eight charged planes, respectively; in particular, we have $z_2 = z_3$, $z_4 = z_5 = z_6$, $z_7 = z_8$.

Conflict of Interest

The authors declare no conflict of interest.

Data Availability Statement

The data that support the findings of this study are available from the corresponding author upon reasonable request.

[1] A. Y. Li, Y. L. Zi, H. Y. Guo, Z. L. Wang, *Nat. Nanotechnol.* **2017**, *12*, 481.

[2] Z. L. Wang, *Rep. Prog. Phys.* **2021**, *84*, 096502.

[3] R. D. I. G. Dharmasena, K. D. G. I. Jayawardena, C. A. Mills, J. H. B. Deane, J. V. Anguita, R. A. Dorey, S. R. P. Silva, *Energy Environ. Sci.* **2017**, *10*, 1801.

[4] H. Wu, N. Mendel, D. van den Ende, G. Zhou, F. Mugele, *Phys. Rev. Lett.* **2020**, *125*, 078301.

[5] W. Xu, H. Zheng, Y. Liu, X. Zhou, C. Zhang, Y. Song, X. Deng, M. Leung, Z. Yang, R. X. Xu, Z. L. Wang, X. Z. Zeng, Z. Wang, *Nature* **2020**, *578*, 392.

[6] R. Hinchet, H.-J. Yoon, H. Ryu, M.-K. Kim, E.-K. Choi, D.-S. Kim, S.-W. Kim, *Science* **2019**, *365*, 491.

[7] Z. L. Wang, *Mater. Today* **2017**, *20*, 74.

[8] Z. L. Wang, *Nano Energy* **2020**, *68*, 104272.

[9] Z. L. Wang, *Mater. Today* **2022**, *52*, 348.

[10] J. Shao, M. Willatzen, Z. L. Wang, *J. Appl. Phys.* **2020**, *128*, 111101.

[11] M. E. Tobar, B.T. McAllister, M. Goryachev, *Phys. Rev. Applied* **2021**, *15*, 014007.

[12] M. E. Tobar, R. Y. Chiao, M. Goryachev, Active Electric Dipole Energy Sources: Transduction via Electric Scalar and Vector Potentials, arXiv:2101.00945.

[13] M. E. Tobar, B. T. McAllister, M. Goryachev, *Phys. Dark Universe* **2019**, *26*, 100339.

[14] D. J. Griffiths, in *Introduction to Electrodynamics*, Prentice Hall, Upper Saddle River, New Jersey **1999**, p.*07458*.

[15] G. M. Sessler, *Electrets*, Springer-Verlag, New York, Berlin, Heidelberg, **1987**.

[16] O. D. Jefimenko, D. K. Walker, *Phys. Teach.* **1980**, *18*, 651.

[17] C. Jean-Mistral, T. Vu Cong, A. Sylvestre, *Appl. Phys. Lett.* **2012**, *101*, 162901.

[18] R. E. Harrington, in *Introduction to Electromagnetic Engineering*, Dover Publications, Inc, East 2nd Street, Mineola, NY **2012**, p. 11501.

[19] J. Shao, D. Liu, M. Willatzen, Z. L. Wang, *Appl. Phys. Rev.* **2020**, *7*, 011405.

[20] J. Shao, Y. Yang, O. Yang, J. Wang, M. Willatzen, Z. L. Wang, *Adv. Energy Mater.* **2021**, *11*, 2100065.

[21] J. J. Shao, M. Willatzen, Y. Shi, Z. L. Wang, *Nano Energy* **2019**, *60*, 630.

[22] X. Guo, J. J. Shao, M. Willatzen, Y. Yang, Z. L. Wang, *Nano Energy* **2022**, *92*, 106762.

[23] X. Guo, J. J. Shao, M. Willatzen, Y. Yang, Z. L. Wang, *J. Phys. D: Appl. Phys.* **2022**, *55*, 345501.

[24] R. D. I. G. Dharmasena, J. H. B. Deane, S. R. P. Silva, *Adv. Energy Mat.* **2018**, *8*, 1802190.

[25] H. T. Baytekin, A. Z. Patashinski, M. Branicki, B. Baytekin, S. Soh, B. A. Grzybowski, *Science* **2011**, *333*, 308.

[26] S. M. Niu, Z. L. Wang, *Nano Energy* **2015**, *14*, 161.

[27] J. You, J. J. Shao, Y. H. He, F. F. Yun, K. W. See, Z. L. Wang, X. L. Wang, *ACS Nano* **2021**, *15*, 8706.

[28] J. J. Shao, M. Willatzen, T. Jiang, W. Tang, X. Y. Chen, J. Wang, Z.L. Wang, *Nano Energy* **2019**, *59*, 380.

[29] D. J. Lacks, T. Shinbrot, *Nat. Rev. Chem.* **2019**, *3*, 465.

[30] B. D. Terris, J. E. Stern, D. Rugar, H. J. Mamin, *Phys. Rev. Lett.* **1989**, *63*, 2669.

[31] Z. L. Wang, L. Lin, J. Chen, S. M. Niu, Y. L. Zi, *Triboelectric Nanogenerators*, Springer, Berlin **2016**.

[32] S. M. Niu, Y. Liu, X. Y. Chen, S. H. Wang, Y. S. Zhou, L. Lin, Y. N. Xie, Z. L. Wang, *Nano Energy*, **2015**, *12*, 760.

[33] Y. L. Zi, J. Wang, S. H. Wang, S. M. Li, Z. Wen, H. Y. Guo, Z. L. Wang, *Nat. Commun.* **2016**, *7*, 10987.

[34] R. Liu, Z. L. Wang, K. Fukuda, T. Someya, *Nat. Rev. Mater.* **2022**, *7*, 870.

[35] M. Willatzen, L. C. Lew Yan Voon, *Separable Boundary-Value Problems in Physics*, Wiley-VCH Verlag GmbH & Co. KGaA, Weinheim, Germany **2011**.